

# Residual-Stress Predictions in Polycrystalline Alumina

Venkata R. Vedula<sup>\*,†</sup> and S. Jill Glass<sup>\*</sup>

Ceramic Materials Department, Sandia National Laboratories, Albuquerque, New Mexico 87185

David M. Saylor<sup>\*</sup> and Gregory S. Rohrer<sup>\*</sup>

Department of Materials Science and Engineering, Carnegie Mellon University, Pittsburgh, Pennsylvania 15213

W. Craig Carter<sup>\*</sup>

Department of Materials Science and Engineering, Massachusetts Institute of Technology, Cambridge, Massachusetts 02139

Stephen A. Langer and Edwin R. Fuller Jr.<sup>\*</sup>

National Institute of Standards and Technology, Gaithersburg, Maryland 20899

**Microstructure-level residual stresses occur in polycrystalline ceramics during processing, as a result of thermal expansion anisotropy and crystallographic misorientation across the grain boundaries. Depending on the grain size, the magnitude of these stresses can be sufficiently high to cause spontaneous microcracking when cooled from the processing temperature. They are also likely to affect where cracks initiate and propagate under macroscopic loading. The magnitudes of residual stresses in untextured and textured alumina samples have been predicted using experimentally determined grain orientations and object-oriented finite-element analysis. The crystallographic orientations have been obtained using electron-backscattered diffraction. The residual stresses are lower and the stress distributions are narrower in the textured samples, in comparison with those in the untextured samples. Crack initiation and propagation also have been simulated, using a Griffith-like fracture criterion. The grain-boundary-energy:surface-energy ratios required for computations are estimated using atomic-force-microscopy thermal-groove measurements.**

## I. Introduction

RESIDUAL stresses form in polycrystalline ceramics during processing, as a result of thermal expansion anisotropy and crystallographic misorientation across the grain boundaries. During formation of the microstructure, boundaries with higher mobilities and energies are likely to be eliminated, thereby changing the distribution of lattice orientations and misorientations. This process is expected to change the distribution of grain orientations (and misorientations) with increasing grain size to a distribution that is less random. Therefore, the magnitude and

distribution of stresses are likely to be dependent on the grain size and degree of texture in the samples.

When a polycrystalline material with noncubic crystal symmetry is subjected to a temperature change, each grain will attempt to strain differently than its neighbors, resulting in residual stresses and strains in the material. In brittle materials, the thermal strains that result during cooling from the sintering temperature can be comparable to the fracture strain of the material, leading to internal cracking (also known as spontaneous microcracking). The onset of microcracking is dependent on the grain (crystal) size; below a critical value, no spontaneous microcracking occurs. Although the stresses generated in a material are not dependent on the grain size, the ability of the material to convert the total strain energy to fracture energy is grain-size-dependent. Assuming that enough stress and potential microcrack formation sites are available, the formation of microcracks in ceramics has been shown to be governed by the stored elastic strain energy.<sup>1</sup>

Highly textured microstructures have been shown to reduce the residual stresses and cracking associated with thermal contraction anisotropy in alumina drastically.<sup>2</sup> More recently, it has also been shown that, under multiple Hertzian indentation loadings, the damage evolution rate is much lower for textured samples.<sup>3</sup> In addition to grain size and texture in samples, grain-shape distribution and the extent to which stress relaxation mechanisms are active will also influence the variation of residual stresses. However, for the purpose of this paper, no stress relaxation mechanisms are assumed to be active.

Residual stresses are critical to the *R*-curve behavior that occurs in some ceramics. In ceramic-containing components, macroscopic residual stresses also result, because of thermal-expansion mismatch between different materials.<sup>4</sup> The interaction between macroscopic and microscopic residual stresses can significantly influence the crack initiation and propagation in the ceramic and affect the component reliability.

This paper presents a methodology to predict residual stresses in ceramics, using experimentally determined grain orientations in conjunction with object-oriented finite-element analysis (OOF). The critical temperature for microcrack formation in alumina is also predicted, as a function of grain size. Crystallographic orientations and relative grain boundary energies required for predictions are obtained using electron-backscattered diffraction (EBSD) and atomic force microscopy (AFM), respectively. The stresses and stress distributions in untextured and textured alumina are compared. A recent study applied a similar approach to predict residual stresses in

J. Rödel—contributing editor

Manuscript No. 188662. Received March 27, 2000; approved August 1, 2001. Sandia is a multiprogram laboratory operated by Sandia Corp., a Lockheed Martin Co., for the United States Department of Energy, under Contract No. DE-ACO4-94AL85000. The work performed at CMU was supported in part by the MRSEC Program of the NSF, under Award Number DMR-9632556.

<sup>\*</sup>Member, American Ceramic Society.

<sup>†</sup>Present address: United Technologies Research Center, East Hartford, CT 06108.

alumina, using computationally generated microstructures and randomly assigned grain orientations.<sup>5</sup>

## II. Experimental Details

### (1) Materials Studied

The untextured samples used in this study were obtained from D. Kovar at the University of Texas at Austin (Austin, TX). The samples were prepared from 99.99%-pure alumina powder (AKP-50, Sumitomo Chemical America, New York).<sup>‡</sup> The powder was compacted in a uniaxial press at 28 MPa and then isostatically pressed at 280 MPa. The pressed pellets were packed in a crucible with the parent powder and fired at 1600°C. Two sets of samples, with average sizes of 10 and 27  $\mu\text{m}$ , were produced. Details of the processing can be found elsewhere.<sup>6</sup> Surfaces of the samples were prepared using an automatic polisher (Model PM5, Logitech, Ltd., Westlake, OH). The samples were initially lapped with 9- $\mu\text{m}$  alumina slurry, followed by a final polish with 0.05- $\mu\text{m}$  colloidal silica (pH 10).

The textured alumina samples were obtained from D. Brandon (Technion—Israel Institute of Technology, Haifa, Israel). They were prepared by gelcasting lay-up tapes that contained aligned alumina platelets. The final microstructure had non-equiaxed, platelike grains and a very strong preferred orientation with the *c*-axis perpendicular to the plane of the tapes.<sup>7</sup> Typical grain dimensions were 28.5  $\mu\text{m}$   $\times$  4.7  $\mu\text{m}$ .

### (2) Electron-Backscattered-Diffraction Measurements

The orientations of individual grains on the surface of samples were obtained using electron-backscattered diffraction (EBSD). The technique involves use of an electron beam incident on a sample tilted at 70° to the electron-beam normal. The interaction of the electron beam with the sample generates a diffraction cone that can be recorded on a phosphor screen. The patterns (known as Kikuchi diffraction patterns) can be indexed to determine the orientation of each grain, with reference to a reference axis. The patterns were collected using scanning electron microscopy (SEM) (Model XL40FEG, Philips Research Laboratories, Eindhoven, The Netherlands). Scans were performed in a hexagonal grid with a spacing of 3 and 1.5  $\mu\text{m}$  in untextured and textured samples, respectively. The grid of measured orientations defines the position and size of each grain. A commercially available system, Orientation Imaging Microscopy<sup>®</sup> (OIM) (TexSEM Laboratories, Inc., Draper, UT) was used to collect and index the patterns automatically. This system allows a large population of grains to be identified.

### (3) Atomic-Force-Microscopy Groove Measurements

The width and depth of the thermal grooves formed at the grain boundaries were measured using atomic force microscopy (AFM), to determine the ratio of the grain-boundary free energy ( $\gamma_{\text{gb}}$ ) to the surface free energy ( $\gamma_s$ ).<sup>8</sup> Dihedral angles were measured using a stand-alone AFM apparatus (Model SAA-125, Digital Instruments, Tonawanda, NY) that was positioned above the sample mounted on an *X*–*Y* translation stage (Model TSE-150, Burleigh Instruments, Fishers, NY) with a reproducible position resolution of 50 nm. (Readers are referred to the work of Saylor and Rohrer<sup>8</sup> for a detailed description of the method.) The samples were thermal-grooved at 1600°C for 100 h. The ratio  $\gamma_{\text{gb}}/\gamma_s$  was obtained using the simplified Herring equation:  $\gamma_{\text{gb}}/\gamma_s = 2 \cos(\psi/2)$ , where  $\psi$  is the surface dihedral angle.<sup>8</sup> This equation assumes that the surface energies are isotropic, the grain-boundary plane is perpendicular to the macroscopic sample surface, and the

grain-boundary energy is a function of misorientation alone and not a function of the boundary-plane inclination.

## III. Finite-Element Analysis

### (1) Object-Oriented Finite-Element Analysis

Object-oriented finite-element analysis (OOF) was developed at NIST.<sup>9,10</sup> It is designed to investigate the response of microstructures to mechanical and thermal loads. The program performs thermoelastic calculations in two dimensions (plane strain or plane stress) using three-node triangular elements. Several “smart” meshing schemes, based on energy minimization, are available to mesh curved features, such as grain boundaries. A digital image of a microstructure, obtained either via optical/electron microscopy or as a result of a computer simulation, can be used for analysis. The crystallographic orientations obtained via EBSD were input manually as a set of Euler angles ( $\alpha$ ,  $\beta$ ,  $\gamma$ ). The elastic stiffness constants used for  $\alpha$ -alumina (trigonal crystal symmetry) in the analysis were as follows:  $C_{11} = 497$  GPa,  $C_{12} = 163$  GPa,  $C_{13} = 111$  GPa,  $C_{14} = -23.5$  GPa,  $C_{33} = 498$  GPa, and  $C_{44} = 147$  GPa. The coefficients of thermal expansion (CTEs) used for  $\alpha$ -alumina in the analysis were as follows:  $\alpha_{11} = 8.6 \times 10^{-6}/^\circ\text{C}$  and  $\alpha_{33} = 9.3 \times 10^{-6}/^\circ\text{C}$ .<sup>11</sup> Based on this data, a finite-element grid with associated properties is generated on which mechanical and/or thermal loading can be applied. Then, a solution is obtained for the specified boundary conditions, distortion, and temperature change. The calculations were performed assuming that the plane stress ( $\sigma_{33} = 0$ ) and free boundary conditions mimicked unconstrained cooling of a thin plate from its sintering temperature.

### (2) OIM-2-OOF Code

The methodology of manually assigning properties to various grains in a microstructure works well when working with smaller microstructures ( $\leq 100$  grains). The objective of this work was to analyze stresses and stress distributions in large microstructures, to gather statistically reliable data. Therefore, an analysis code (OIM-2-OOF) was developed that allows crystallographic orientations from OIM to be directly imported into OOF. An OIM scan is typically conducted in a hexagonal grid, where the user specifies the step size and the *x*- and *y*-axis ranges for the scan. The OIM-2-OOF code converts the data from the hexagonal grid to a square grid, generates an image, and writes an intermediate file that contains information regarding the grains and their respective crystallographic orientations. This code allows the user to analyze residual-stress distributions in large microstructures ( $> 600$  grains) with relative ease. The code also detects grain boundaries and assigns respective relative grain-boundary energies (obtained by groove measurements) automatically.

### (3) Crack Propagation in Ceramics

The elements in the OOF code are designed to fail under a Griffith-like strain-energy-based criterion. The elements crack when the required surface energy can be supplied by the stored strain energy per crack extension ( $\Delta L$ ), i.e.,

$$\frac{1}{2} \sigma_{ij}^{\text{elem}} \epsilon_{ij}^{\text{elem}} \frac{A_{\text{elem}}}{\Delta L} \geq 2\gamma \quad (1)$$

where  $A_{\text{elem}}$  is the element area and  $\gamma$  is the surface energy of the cracked interface;  $\sigma_{ij}^{\text{elem}}$  and  $\epsilon_{ij}^{\text{elem}}$  are the respective stresses and strains in the elements.

The analysis involves the following steps:

(1) Thermal and mechanical loads are applied and the microstructure is equilibrated to determine stress/strain distribution.

(2) The energy balance is computed and, if an element satisfies the energy criterion for cracking, the stiffness of the element is set to zero.

(3) The microstructure is re-equilibrated and the stress distribution is recalculated.

<sup>‡</sup>Certain trade names and company products are mentioned in the text to specify the experimental procedure and equipment used adequately. In no case does such identification imply recommendation or endorsement by the National Institute of Standards and Technology, nor does it imply that the products are necessarily the best available for that purpose.

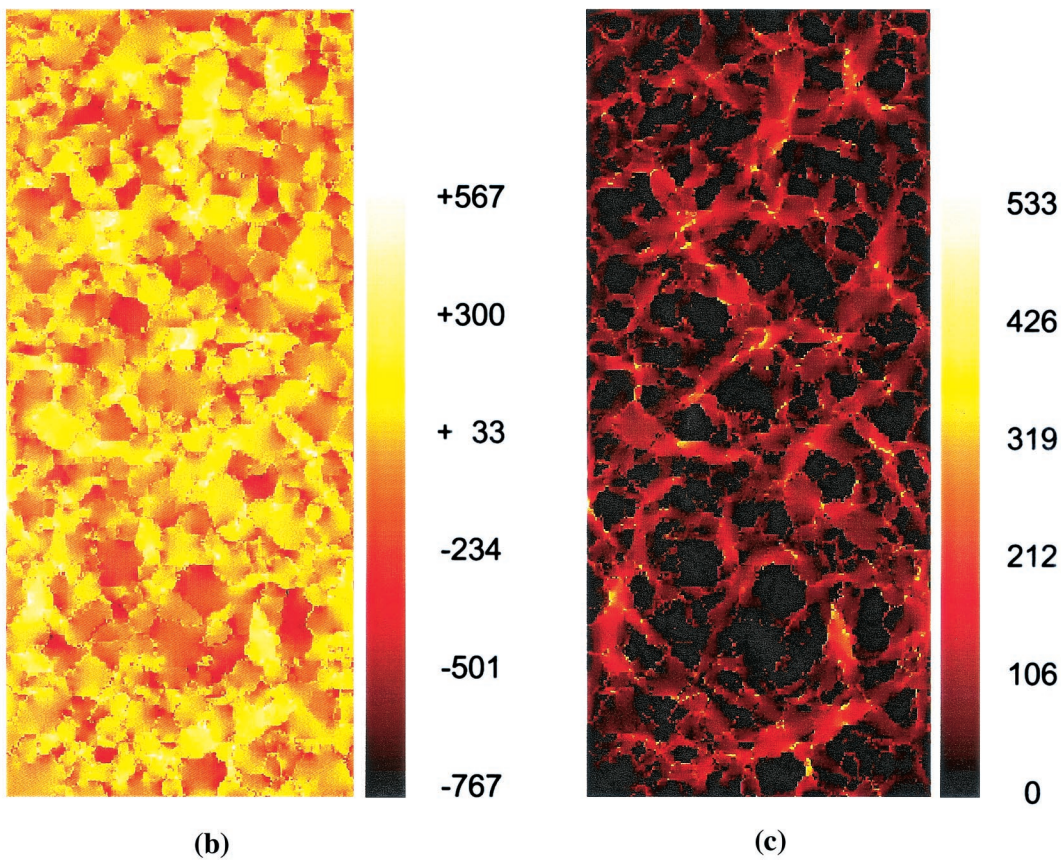
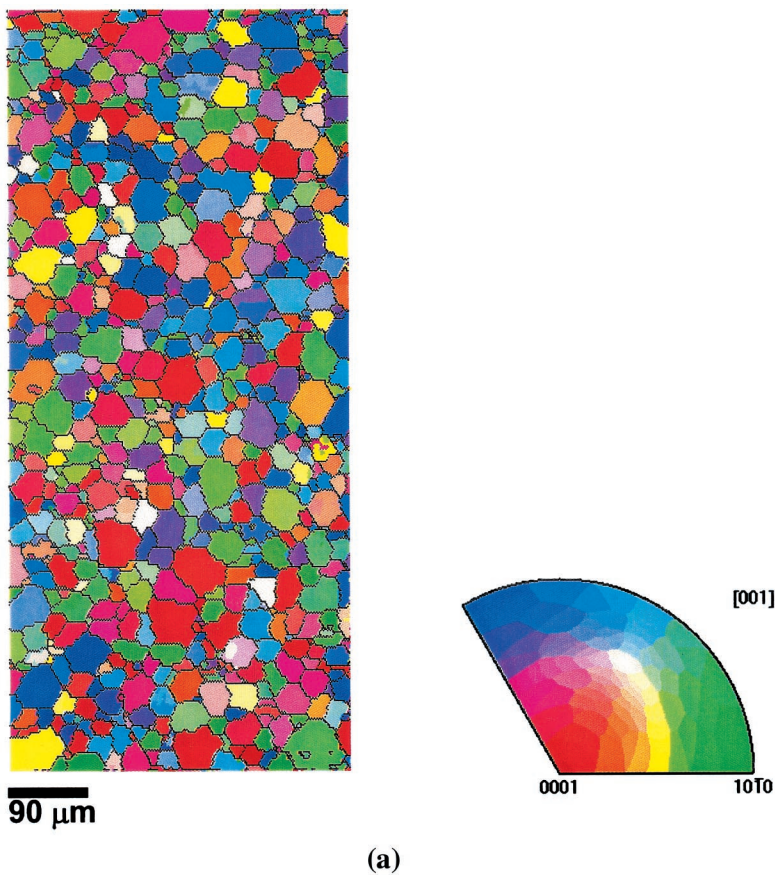


**Fig. 1.** Residual-stress distribution in untextured alumina when  $\Delta T = -1500^\circ\text{C}$  ((a) microstructure with grain normals given by the stereographic triangle, (b) stress invariant I ( $\sigma_{11} + \sigma_{22}$ ), and (c) maximum principal stress ( $\sigma_{11}$ )). Values in Figs. 1(b) and (c) are given in MPa.

(4) Steps (1)–(3) are repeated until no more elements mutate or one or more cracks become unstable, causing fracture into two or more fragments.

#### IV. Results and Discussion

##### (1) Residual-Stress Distributions in Untextured and Textured Alumina

Residual stresses in alumina (~650 grains) that are due to its thermal-expansion anisotropy were estimated using the OIM-2-OOF and OOF codes. The OIM orientation map of the untextured microstructure (grain size of 27  $\mu\text{m}$ ) is shown in Fig. 1(a). The grains are color-coded, where each color represents an orientation normal to the specimen surface, as shown by the stereographic triangle in the figure. The pole figures from EBSD data showed a maximum multiples-of-random-distribution (MRD) value of 2. The OOF simulation used 117 612 elements. Figure 1 shows the microstructure (OIM output), stress invariant 1 ( $\sigma_{11} + \sigma_{22}$ ), and maximum-principal-stress distribution for a temperature change of  $\Delta T = -1500^\circ\text{C}$ . The highest maximum principal stress was fairly large (~530 MPa). The highest stresses were localized at the grain boundaries and triple junctions and four-grain junctions and decrease rapidly away from the boundaries, as shown by the example of two adjoining grains in Fig. 2. The residual-stress distributions were almost identical in the 10- and 27- $\mu\text{m}$  samples, which indicates that grain size has a negligible effect (orientations were random in both cases). The stresses within the grains (~100–200 MPa) compare favorably with those measured via spectroscopic<sup>12</sup> and fluorescence imaging.<sup>13</sup> Regions of high tensile and compressive stresses seem to exist on a scale that is larger than the grain size (Fig. 1). To test the idea that these regions were correlated to local orientation correlations, an orientation-averaging procedure was developed. The description of the orientation of each element was reduced to a single parameter ( $q$ ) with a range of  $0-\pi/2$ , which denotes the angle between the  $c$ -axis and the vector normal to the macroscopic sample surface. Then, the orientation at each element was recalculated as the average of all  $q$  values in an  $N \times M$  element area centered on the element, where the  $N \times M$  area is larger than the grain size. Two-dimensional plots that show the spatial variation of the average orientation showed regions of similar  $q$  values that were larger than the grain size and strongly correlated to the distribution of maximum principal stress in Fig. 1(c). The regions with low  $q$  values, or near  $c$ -axis orientations, had relatively low maximum principal stresses (in compression) associated with them, whereas regions with high  $q$  values were regions of relatively high maximum principal stress (in tension). Analysis is continuing to attempt to quantify these observations.

Residual stresses were also predicted for textured alumina. The sample had a  $c$ -axis texture with a maximum MRD value of 90. The number of grains and the total number of elements

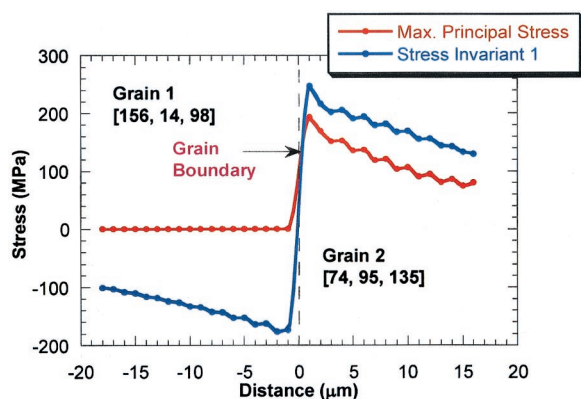


Fig. 2. Change in residual stress across a grain boundary for two grains (Euler angles are shown in brackets).

(117 612) were the same as those used to analyze the untextured sample. As one would expect, the stresses were much smaller in this sample, in comparison with randomly oriented samples. The largest maximum principal stress was ~415 MPa. Figure 3 shows the microstructure, stress invariant 1, and maximum principal stress for a temperature change of  $\Delta T = -1500^\circ\text{C}$ . The number of elements versus their stress value (stress invariant 1) is plotted for both textured and untextured sample in Fig. 4. The number of elements with high stresses is much smaller in the textured sample than in the untextured sample. In both cases, the number of elements with high stresses is very small. In the untextured sample, <5% of the total elements had high stresses (greater than 250 MPa and less than -250 MPa). The corresponding number in the textured sample was <0.4%.

Stress predictions were also made on periodic equiaxed microstructures that were generated by the Pott's model<sup>14</sup> to validate the boundary conditions. The residual stresses in the original microstructure and a periodic microstructure with a periodicity of  $3 \times 3$  (9 times larger than the original image) were compared using free boundary conditions. The stresses and stress distributions obtained in both cases were almost identical, which indicates that free boundary conditions (free edges) do not lead to any artificial effects.

Note that the stress calculations are purely elastic and assume that no stress-relaxation mechanisms are active. In reality, diffusional flow, plastic deformation, and microcracking will relax the constraints between the grains and reduce the residual stresses.

##### (2) Crack Initiation and Propagation

In brittle materials such as ceramics, cooling from the sintering temperature (~1550°C for alumina) can create sufficiently high stresses to cause microcracking. This microcracking behavior, which is due to thermal-expansion anisotropy, exhibits a critical grain-size relationship. For a given temperature decrement (critical temperature  $T_c$ ), specimens with grain sizes larger than a critical size have been shown experimentally to experience microcracking, whereas specimens with smaller grain sizes do not.<sup>15,16</sup> The microcrack initiation and propagation and the effect of grain size on cracking was determined using the microstructure shown in Fig. 5.

The energy required for crack propagation through a grain is denoted as  $2\gamma_s$ , and that through a grain boundary (intergranular) is defined as  $2\gamma_{ig} = (2\gamma_s - \gamma_{gb})$  (where  $\gamma_s$  is the surface energy of grains and  $\gamma_{gb}$  is the grain-boundary energy). The surface energy of grains was taken as  $\gamma_s = 2 \text{ J/m}^2$ . AFM measurements were made on every boundary in Fig. 5, and the value of  $\gamma_{ig}$  varied over a range of 0.59–1.17  $\text{J/m}^2$ , with an average value of 0.89  $\text{J/m}^2$ . The grain-boundary elements were assigned the elastic properties of glass (isotropic crystal symmetry): elastic modulus of  $E = 70 \text{ GPa}$ , CTE of  $\alpha = 9.5 \times 10^{-6}/^\circ\text{C}$ , and Poisson's ratio of  $\nu = 0.23$ . The elements in the model that represent grains were assigned a surface energy of  $\gamma_s = 2 \text{ J/m}^2$  and the boundary elements were assigned their respective  $\gamma_{ig}$  values. The surface-energy anisotropy in alumina has been reported to be ~12% at 1600°C.<sup>17</sup> However, in the present analysis, the surface energy of alumina is assumed to be isotropic.

Microcrack propagation was simulated with an increasing temperature difference using the procedure described in Section III(3). Figure 5 shows the initiation of microcracks at the triple junctions when  $\Delta T$  has a value between  $-925^\circ\text{C}$  and  $-1500^\circ\text{C}$ . The largest stress intensification has been shown numerically to occur at the triple junctions.<sup>18</sup> When the temperature difference (thermal strain) increased, microcracks initiated at new sites and a coalescence of microcracks was also observed to form large cracks. As can be observed, damage occurred at several regions and some of the boundaries were completely cracked.

The effect of grain size on the critical temperature for microcracking in alumina was also determined using the microstructure in Fig. 5 by varying the dimensions of the image;

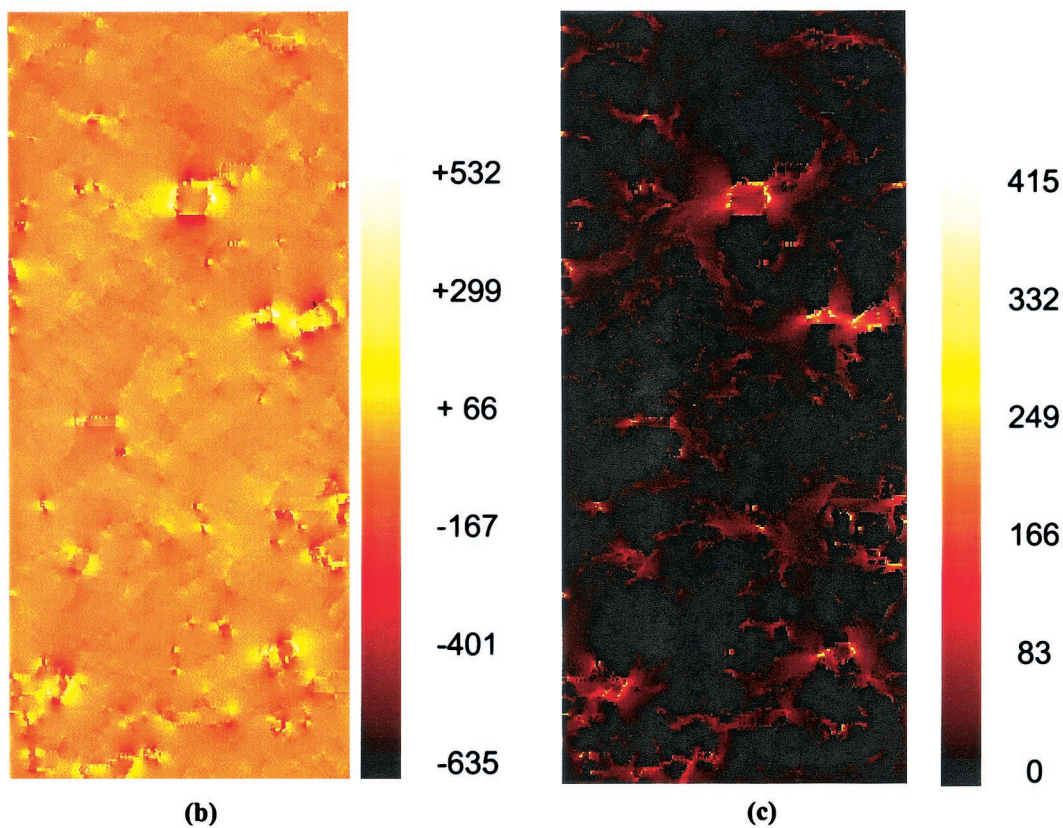
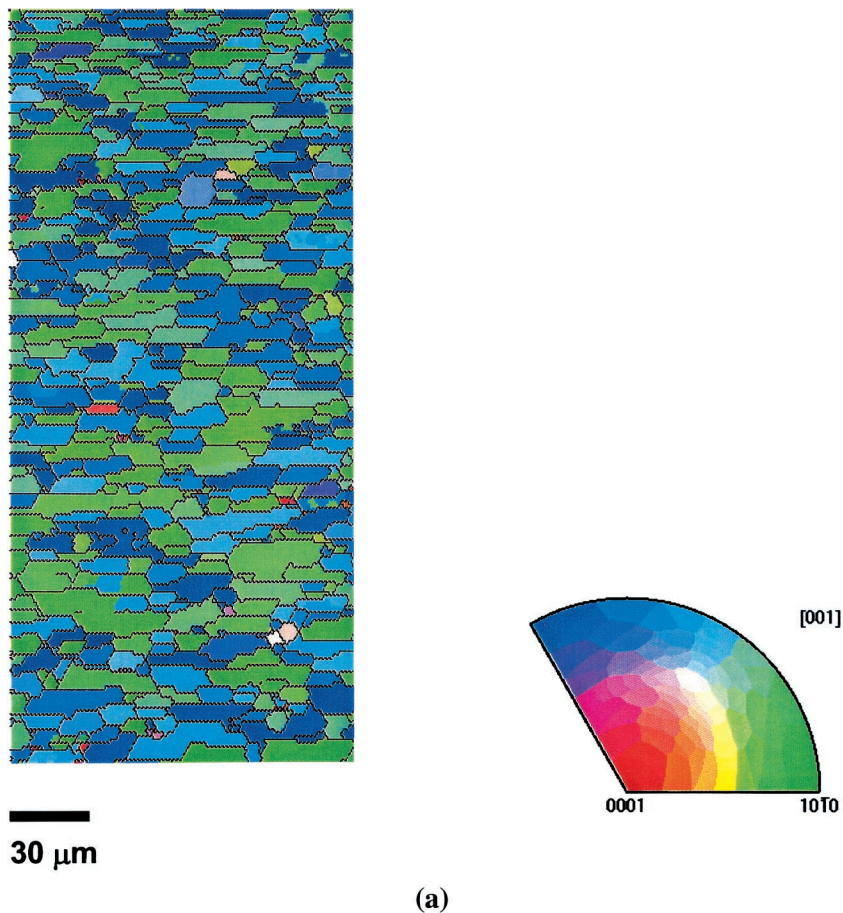


**Fig. 3.** Residual-stress distribution in textured alumina when  $\Delta T = -1500^\circ\text{C}$  ((a) microstructure with grain normals given by the stereographic triangle, (b) stress invariant 1 ( $\sigma_{11} + \sigma_{22}$ ), and (c) maximum principal stress ( $\sigma_{11}$ )). Values in Figs. 3(b) and (c) are given in MPa.

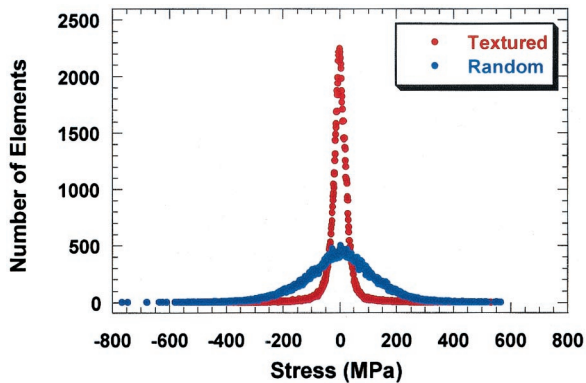


**Fig. 4.** Residual-stress distribution in textured and randomly oriented alumina samples, showing the number of elements versus stress (stress invariant 1).

i.e., different length scales were used to represent different grain sizes. The fracture criterion can be implemented either by scaling up the finite-element mesh along with the microstructure or by maintaining a constant element size. In the first case, the element size (area) is proportional to the square of the average grain size (gs):  $A_{\text{elem}} \propto (\Delta L)^2 \propto (\text{gs})^2$ . Therefore, the microcracking criterion is mesh-dependent, because, from Eq. (1),

$$2\gamma \leq \frac{1}{2} \sigma_{ij}^{\text{elem}} \epsilon_{ij}^{\text{elem}} \frac{A_{\text{elem}}}{\Delta L} \propto \frac{1}{2} \sigma_{ij}^{\text{elem}} \epsilon_{ij}^{\text{elem}} \Delta L \quad (2)$$

Also, the residual stresses and strains are proportional to  $\Delta T$  and the above-described criterion can be rewritten as

$$\frac{1}{2} \sigma_{ij}^{\text{elem}} \epsilon_{ij}^{\text{elem}} \Delta L \propto (\Delta T)^2 (\text{gs}) \geq 2\gamma \quad \text{or} \quad \Delta T \propto \frac{1}{(\text{gs})^{1/2}} \quad (3)$$

Hence, any physical effect can only be found if the same element size is used in both fine- and coarse-grained structures. In the simulations, coarse-grained microstructures were generated by enlarging the original structure. However, the element size was kept constant.

The properties of the grain-boundary glass phase are expected to influence the stress distribution and critical temperature for microcracking. Two different glass compositions were considered for the grain-boundary phase, namely, a high-CaO glass and a high-MgO glass. A high-CaO glass has a CTE of  $\alpha \approx 9.5 \times 10^{-6}/^\circ\text{C}$ , which results in tensile residual stresses at grain boundaries, whereas for a high-MgO glass ( $\alpha \approx 5 \times 10^{-6}/^\circ\text{C}$ ), compressive stresses result at the grain boundaries.<sup>19</sup> These compositions and associated properties were chosen because they represent the bounds on the types of grain-boundary glass phase typically found in alumina. The intergranular fracture energy of all boundaries was assigned a value of 0.89 J/m<sup>2</sup> (average measured value).

Figure 6 shows the effect of grain size on the critical temperature for microcracking. As shown, the data fit the experimentally observed inverse-square-root relationship<sup>16</sup> very well. The critical grain size for microcracking for an alumina sample that has been cooled from a 1600°C sintering temperature with a high-CaO glass ( $\alpha \approx 9.5 \times 10^{-6}/^\circ\text{C}$ ) grain-boundary phase was 188  $\mu\text{m}$ , and that with a high-MgO phase ( $\alpha \approx 5 \times 10^{-6}/^\circ\text{C}$ ) was 29  $\mu\text{m}$  (trend lines in Fig. 6 represent extrapolated values). Experimentally, critical grain sizes of 40–400  $\mu\text{m}$  have been reported.<sup>20,21</sup> Note that plane-stress conditions underestimate the residual stress; hence, in reality, the critical grain sizes are expected to be smaller.

In addition, the grain-size distribution is also likely to influence the critical size for microcracking. It was reported recently that large grains may be in favorable orientations with

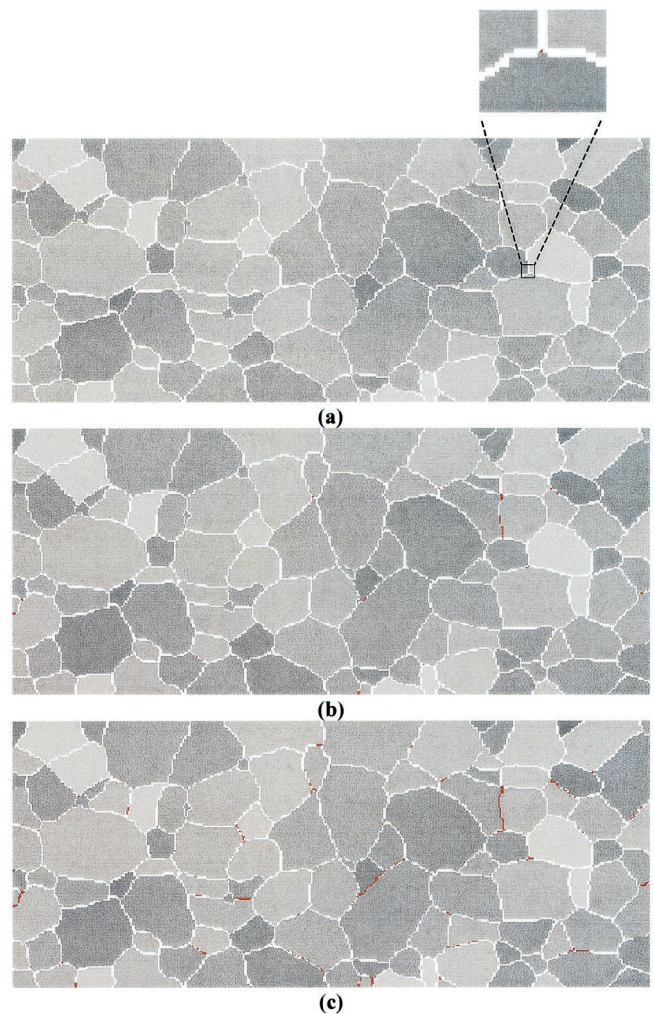


**Fig. 5.** Microstructures of untextured alumina showing different grains. Figures indicate microcrack initiation and propagation with increasing temperature difference. First crack initiated at  $-925^\circ\text{C}$ . Figures 5(a), (b), and (c) show cracks (elements in red) at  $\Delta T = -925^\circ\text{C}$ ,  $-1200^\circ\text{C}$ , and  $-1500^\circ\text{C}$ , respectively.

their neighbors and, therefore, may have little stress concentration at their grain boundaries.<sup>5</sup> Similar qualitative observations have been made in the present study, where more cracks are observed around small grains than large grains. It is important to note that, in addition to stresses, other factors that determine the onset of microcracking include the size and location of existing flaws, because these can act as nucleation sites for microcracks. It has been shown that the inverse-square-root relationship observed here for microcrack initiation is valid for damage evolution with increasing misfit strain, and the behavior can be described by a three-parameter Weibull distribution.<sup>22</sup>

### (3) Effect of Grain-Boundary Thickness

In the above-described crack-propagation analysis, it was assumed that, when the glass phase is present, all grain boundaries are wet and the boundary thickness is constant. The wetting of interfaces and the thickness of boundaries have been shown to be far more complicated. The wetting behavior is dependent on the crystal misorientation and boundary orientation,<sup>23</sup> and the thickness of the grain-boundary phase, when it exists, is on the order of 1–10 nm.<sup>24</sup> Three-dimensional Wulff constructions have shown that transitions from dry to partially wetted to fully wetted boundaries are dependent on the grain-boundary misorientation, grain-boundary-plane orientation, and the energies of the grain

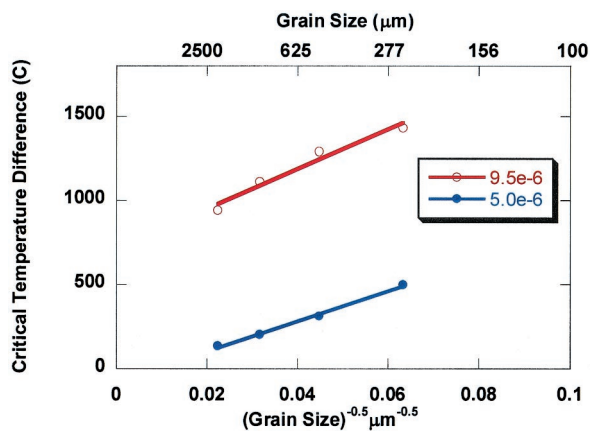


Fig. 6. Critical temperature difference versus grain size in alumina for two different grain-boundary-glass properties (high-CaO glass,  $\alpha = 9.5 \times 10^{-6}/^{\circ}\text{C}$  and high-MgO glass,  $\alpha = 5 \times 10^{-6}/^{\circ}\text{C}$ ).

boundary and the wetted interface.<sup>25</sup> The initial separation between crystalline particles is also likely to have a role in the presence and thickness of grain-boundary films.<sup>26</sup>

Because of computational limitations, a nanometer-scale grain boundary could not be considered in the above-mentioned analysis (Fig. 5). A set of calculations was obtained on a smaller microstructure, to determine the effect of the boundary thickness on residual stresses and the critical temperature for microcracking (Fig. 7). The thickness of the boundary was varied over a range of 20–100 nm, and the grain boundary was assumed to be a high-CaO glass phase ( $\alpha \approx 9.5 \times 10^{-6}/^{\circ}\text{C}$ ). The mesh size and the number of elements (379 904) were maintained constant in the calculations. Table I shows the effect of thickness on stress. As the thickness decreases, the stresses increase, which is intuitive as the constraint on the grain boundary from neighboring grains increases. The critical temperature is also expected to increase as the thickness increases. We observed that this phenomenon is related to the changes in the stress and strain-energy density in the boundary region. Note that the effects of stress relaxation and grain-boundary thickness counteract each other; therefore, the use of an artificially thicker grain boundary compensates, at least in part, for the stress-relaxation effects that are not considered in the analysis.

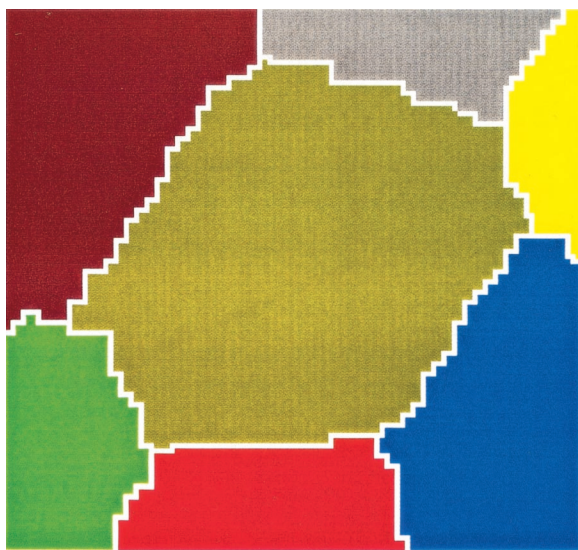


Fig. 7. Microstructure used to evaluate the effect of boundary thickness on residual stresses and microcrack initiation.

Table I. Effect of Grain-Boundary Thickness on Residual Stresses in Alumina

Thickness (nm)	Stress invariant I (MPa)	Maximum principal stress (MPa)
20	379 to -569	318
60	324 to -596	271
100	285 to -593	237

## V. Conclusions

This study is the first to predict residual stresses in alumina using measured experimental grain orientations. The magnitudes of residual stresses in untextured and textured alumina were predicted using object-oriented finite-element analysis and experimentally determined orientations. The stresses were very high and localized at the grain boundaries. The residual stresses were lower and the stress distributions were narrower in textured samples, in comparison with those properties in untextured samples. Microcrack initiation was simulated using a strain-energy-based criterion and measured grain-boundary energies. The increase in damage, relative to an increasing temperature difference, occurred via both the formation of new cracks and the propagation of existing cracks.

## Acknowledgments

The authors would like to acknowledge Ming Wei and Profs. David Brandon and Desiderio Kovar for the samples used in this study.

## References

- J. A. Kuszyk and R. C. Bradt, "Influence of Grain Size on Effects of Thermal Expansion Anisotropy in  $\text{MgTi}_2\text{O}_7$ ," *J. Am. Ceram. Soc.*, **56** [8] 420–23 (1973).
- T. Carisey, I. Levin, and D. G. Brandon, "Microstructure and Mechanical Properties of Textured  $\text{Al}_2\text{O}_3$ ," *J. Eur. Ceram. Soc.*, **15** [4] 283–89 (1995).
- L. An, "Indentation Fatigue in Random and Textured Alumina Composites," *J. Am. Ceram. Soc.*, **82** [1] 178–82 (1999).
- V. R. Vedula, S. J. Glass, S. L. Monroe, and C. Newton, "Reliability and Lifetime Predictions for Ceramic Components," *Ceram. Eng. Sci. Proc.*, **20** [3] 589–94 (1999).
- A. Zimmerman, E. R. Fuller, and J. Rödel, "Residual Stress Distributions in Ceramics," *J. Am. Ceram. Soc.*, **82** [11] 3155–60 (1999).
- D. Kovar, "The Role of Microstructure on the Mechanical Reliability of Alumina Ceramics"; Ph.D. Thesis. Carnegie Mellon University, Pittsburgh, PA, 1995.
- T. Carisey, A. Laugier-Werth, and D. G. Brandon, "Control of Texture in  $\text{Al}_2\text{O}_3$  by Gel-casting," *J. Eur. Ceram. Soc.*, **15**, 1–8 (1995).
- D. M. Saylor and G. S. Rohrer, "Measuring the Influence of Grain-Boundary Misorientation on Thermal Groove Geometry in Ceramic Polycrystals," *J. Am. Ceram. Soc.*, **82** [6] 1529–36 (1999).
- W. C. Carter, S. A. Langer, and E. R. Fuller Jr., *The OOF Manual: Version 1.0*, National Institute of Standards and Technology (NIST), NISTIR No. 6256, Nov. 1998. (Also available as Document No. PB99-118473INZ from National Technical Information Service, Springfield, VA, 22161 and on the Internet at <http://www.ctcms.nist.gov/oof/>.)
- S. A. Langer, E. R. Fuller Jr., and W. C. Carter, "OOF: An Image-based Finite Element Analysis of Material Microstructures," *Comput. Sci. Eng.*, **3** [3] 15–23 (2001).
- J. B. Wachtman, W. E. Tefft, D. G. Lam, and R. P. Stinchfield, "Elastic Constants of Synthetic Single Crystal Corundum at Room Temperature," *J. Res. Natl. Bur. Stand. (U.S.)*, **64A**, 213–28 (1960).
- Q. Ma and D. R. Clarke, "Piezospectroscopic Determination of Residual Stresses in Polycrystalline Alumina," *J. Am. Ceram. Soc.*, **77** [2] 298–302 (1994).
- R. H. Dauskardt and J. W. Ager, "Quantitative Stress Mapping in Alumina Composites by Optical Fluorescence Imaging," *Acta Mater.*, **44** [2] 625–41 (1996).
- D. J. Srolovitz, M. P. Anderson, G. S. Grest, and P. S. Sahni, "Grain Growth in Two-Dimension," *Scr. Metall.*, **17**, 241–46 (1983).
- D. J. Green, *An Introduction to the Mechanical Properties of Ceramics*. Cambridge University Press, Cambridge, U.K., 1998.
- E. D. Case, J. R. Smyth, and O. Hunter, "Grain-Size Dependence of Microcrack Initiation in Brittle Materials," *J. Mater. Sci.*, **15**, 149–53 (1980).
- J.-H. Choi, D.-Y. Kim, B. J. Hockey, S. M. Wiederhorn, C. A. Handwerker, J. E. Blendell, W. C. Carter, and A. R. Roosen, "Equilibrium Shape of Internal Cavities in Sapphire," *J. Am. Ceram. Soc.*, **80** [1] 62–68 (1997).
- A. G. Evans, "Microfracture from Thermal Expansion Anisotropy—I. Single Phase Systems," *Acta Metall.*, **26**, 1845–53 (1978).

<sup>19</sup>C. A. Powell-Dogan and A. H. Heuer, "Microstructure of 96% Alumina Ceramics: III, Crystallization of High-Calcia Boundary Glasses," *J. Am. Ceram. Soc.*, **73** [12] 3684–91 (1990).

<sup>20</sup>E. D. Case, J. R. Smyth, and O. Hunter, "Microcracking in Large Grain  $\text{Al}_2\text{O}_3$ ," *Mater. Sci. Eng.*, **51** [2] 175–79 (1981).

<sup>21</sup>(a) R. W. Rice, S. W. Freiman, and P. F. Becher, "Grain-Size Dependence of Fracture Energy in Ceramics: I, Experiment," *J. Am. Ceram. Soc.*, **64** [6] 345–50 (1981). (b) R. W. Rice and S. W. Freiman, "Grain-Size Dependence of Fracture Energy in Ceramics: II, A Model for Noncubic Materials," *J. Am. Ceram. Soc.*, **64** [6] 350–54 (1981).

<sup>22</sup>A. Zimmermann, W. C. Carter, and E. R. Fuller Jr., "Damage Evolution During Microcracking of Brittle Solids," *Acta Mater.*, **49** [1] 127–37 (2001).

<sup>23</sup>D.-Y. Kim, S. M. Wiederhorn, B. J. Hockey, C. A. Handwerker, and J. E. Blendell, "Stability and Surface Energies of Wetted Grain Boundaries in Aluminum Oxide," *J. Am. Ceram. Soc.*, **77** [2] 444–53 (1994).

<sup>24</sup>D. R. Clarke, "On the Equilibrium Thickness of Intergranular Glass Phases in Ceramic Materials," *J. Am. Ceram. Soc.*, **70** [1] 15–22 (1987).

<sup>25</sup>J. E. Blendell, W. C. Carter, and C. A. Handwerker, "Faceting and Wetting Transitions of Anisotropic Interfaces and Grain Boundaries," *J. Am. Ceram. Soc.*, **82** [7] 1889–900 (1999).

<sup>26</sup>H. D. Ackler and Y.-M. Chiang, "Effect of Initial Microstructure on Final Intergranular Phase Distribution in Liquid Phase Sintered Ceramics," *J. Am. Ceram. Soc.*, **82** [1] 183–89 (1999). □